Original Article

Institution of MECHANICAL ENGINEERS
Journal of MECHANICAL ENGINEERING SCIENCE

Proc IMechE Part C:
J Mechanical Engineering Science
0(0) 1–12

DOI: 10.1177/0954406220917712
journals.sagepub.com/home/pic
SAGE

Assessment of non-uniform residual stress field of the thermal sprayed stainless steel coatings on aluminium substrates by the integral hole drilling method

Harouche Mohamed Karim[1], Hattali Lamine[2] and Mesrati Nadir[3]

Abstract

Thermal spray is one of the most used techniques to produce coatings on structural materials. Such coatings are used as protection against high temperatures, corrosion, erosion and wear. The combined action of high pressures, temperatures and spraying conditions give rise to non-uniform residual stresses. The latter plays an important role in coating design and process parameters optimization. The present work highlights the influence of coatings thickness on the evolution of residual stresses in layered materials. Therefore, thick stainless steel coatings (ASTM 301) of different thicknesses are manufactured by wire arc spraying on aluminium alloy substrates (ASTM 2017A). For a better bond strength, a Ni–Al bond coat is first deposited. Furthermore, a numerically supported hole drilling strain gage method for residual stress field evaluation is proposed. Required calibration coefficients, for the strain–stress transformation formalism based on the integral method, are computed through finite element calculations using Abaqus software. The results indicate that the maximum residual stresses, for all thicknesses, are tensile and range from 140 to 275 MPa. The bond coat does not seem to affect the stress field. Also, it was found that the mean equivalent Von-Mises stress decreases with increasing coating thickness; hence reducing the interfacial adhesion energy of the sprayed materials.

Keywords

Thermal spraying, residual stresses, incremental hole drilling, integral method, metallic coating

Date received: 2 December 2019; accepted: 10 March 2020

Introduction

Thermal spray is a versatile technology which uses different processes such as: wire arc, plasma spraying and high-velocity oxy fuel (HVOF) to produce coatings on engineering materials.[1] There are several applications of this process including tribological, wear-resistant and corrosion resistant coatings, thermal barriers and erosion protection.[2–5]

Among the different sprayed materials, the X10CrNi18-8 austenitic stainless steel (ASTM 301) is of particular interest[6] as it has many industrial applications in manufacturing components for food processing, medical instrumentation and, maritime and aeronautical uses, etc. More precisely, current trends in the engineering industry, such as aircraft and automotive, deal with the production of stainless steel coatings on aluminium alloys. Successful applications of the aforementioned deposits are reported by Sova et al.[7] and Spencer and Zhang.[8]

The elaboration process of thermally sprayed materials systematically introduces residual stresses which influence the global behaviour of the obtained structure.[9,10] Accurate characterization of the stress state is a challenging task since it can have a random through thickness intensity and distribution.[11]

Various experimental techniques exist to assess in-depth residual stress fields. These methods are classified into destructive and non-destructive methods.[12] Substrate curvature measurements combined with

[1]Laboratoire Dynamique des Systèmes Mécaniques, Ecole Militaire Polytechnique, Bordj El Bahri, Algiers, Algeria
[2]Université Paris–Saclay, CNRS, FAST, Orsay, France
[3]Département de Métallurgie, Ecole Nationale Polytechnique d'Alger, Algeria

Corresponding author:
Harouche Mohamed Karim, Laboratoire Dynamique des Systèmes Mécaniques, Ecole Militaire Polytechnique, BP17, Bordj El Bahri 16046, Algiers, Algeria.
Email: mohamedkarim.harouche@emp.mdn.dz

Stoney's equation are successfully applied for stress measurement in the case of thin coatings.[13]

For thick film systems, the used methods are: X-ray diffraction (XRD),[14,15] the modified layer removal method (MLRM)[16,17] and the incremental hole-drilling technique (HDM).[18,19] The latter is one of the most used techniques. Its popularity stems from its ease of use, semi-destructive aspect and general reliability. Due to the combined action of high temperatures and pressures, the in-depth stress field of thermally sprayed materials is often expected to be non-uniform. Such profiles cannot be addressed by the basic formalism of the incremental hole-drilling method described in the existing standards.[20] To overcome this limitation, many authors show a great interest in developing other strain–stress transformation formalisms referred in the literature as: the incremental strain method,[21–23] the average strain method[24] and the integral method.[25–27] A comparative study of these methods was recently done by Lord et al.[28] It was found that the integral method is the most adequate technique to deal with non-uniform stress fields. In fact, the contributions to the total measured strain relaxation of the stress at all depths are simultaneously considered.[29]

In the integral method-based formalism, the calibration coefficients in the relationship of the residual stress and relieved strains are crucial and need to be predetermined. It should be pointed out that, in the cases of blind holes and thin workpieces, no exact solution is yet available to compute these coefficients.[30] Their experimental determination for bulk materials has the disadvantage of being time and materials consuming.[31] However, the finite element calculation of the calibration coefficients opens new possibilities to characterise non-uniform residual stress based on incremental relaxed strain data. Some references highlight the different finite element models for calibration coefficients calculation.[30,32]

The purpose of the work presented here is to examine the effect of coating thickness on the generated residual stresses of ASTM 301/Ni-Al/ASTM 2017A wire arc thermal sprayed systems. The Ni–Al bond coat was deposited to enhance mechanical bonding of the final stainless steel coatings. Therefore, the non-uniform residual stresses were determined by mean of the incremental hole-drilling method, for different thicknesses. Calibration coefficients, for the stress–strain transformation formalism based on the integral method, were obtained by an automatic routine coded in Python language for finite element software Abaqus.

Materials and methods

Coatings deposition

ASTM 2017A aluminium alloy substrates with dimensions 100 mm × 100 mm × 8 mm are coated with an ASTM 301 stainless steel wires of 2 mm in diameter. The adhesion of the coating to the substrate predominantly consists of mechanical bonding; thus, careful cleaning and pretreatment of the surface to be coated are important. In fact, all samples are prepared according to the prescriptions reported in the standard.[33] Surfaces are polished by an abrasive silicon carbide (SiC) paper of increasing grid from 120 μm to 1200 μm and ultrasonically cleaned by acetone and ethanol for 10 min to remove oxide layers.

Specimens are, then, degreased and grit blasted at a mean pressure of 300 KPa. Grit blasting is carried out in order to increase the surface roughness of the samples and improve the mechanical bonding of the coating. The surface roughness of the grit-blasted specimens is analysed by a Bruker Mechanical Profilometer (Dektak-XT) and is found to be Ra ≈25,49 μm. Figure 1 shows an example of a 3D rugosity profile of the sandblasted substrate surface. Then, coatings are deposited on the substrates in an ambient atmosphere in two steps: an Ni–Al bond coat of ≈90 μm thickness followed by a final coating of ASTM 301 stainless steel of different thicknesses. Chemical compositions and basic mechanical properties, obtained from tensile tests, of the used materials are summarized in Tables 1, 2 and 3.

All coatings are industrially deposited in a system of 3, 6, 9 and 12 passes. The spraying process is carried out using an electric Arc spray 234 (Metal Spray Co.Ltd, Aukland, New Zealand). The average deposits thicknesses are found to be (296.27 ± 14.96) μm (344.30 ± 24.89) μm (693.64 ± 43.94) μm and (747.34 ± 26.4) μm, respectively. For residual stress evaluations, above thicknesses are approximated by 300, 350, 700 and 750 μm, respectively. Figure 2(a) shows the cross-sectional microstructure of a coated ASTM 2017A substrate with an approximate 300 μm stainless steel thickness. A layered structure (substrate/bond coat/coating), due to gradual deposition, with several interlamellar pores is identified in Figure 2(b). Spraying parameters and experimental conditions are given in Tables 4 and 5, respectively.

Strain gage installation, drilling sequence and data acquisition

According to the ASTM E837–13 standards, the maximum drilling hole depth is directly related to strain gage size. For a strain gage with a diameter D, relaxed strains are measured as the hole depth is increased up to a final hole depth of 0.4 × D. Greater depths are pointless because the surface strain gages are not sensitive to contributions at subsequent depth increments. Therefore, a general purpose HBM strain gage rosette type (A) 1-RY61-1.5/120 s of 2 mm in diameter, shown in Figure 3(a) and 3(b), is installed in the centre of the specimens. The selected gage diameter allows a maximum investigated depth of 0.4 × 2 = 800 μm. Since the maximum coating thickness (750 μm) is less than 800 μm, all recommendations of

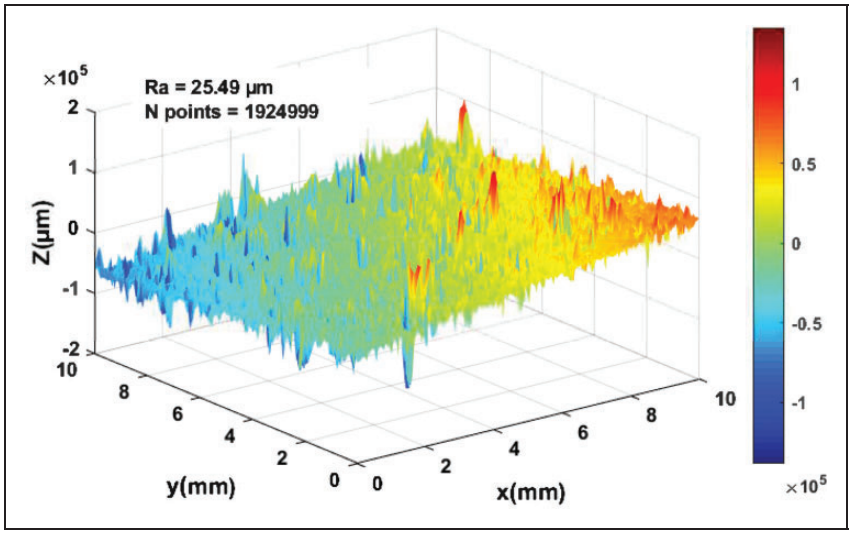

Figure 1. 3D rugosity profile of the sandblasted substrate surface.

Table 1. Mechanical properties of: coating, bond coat and substrate.

	Material	Elastic modulus E(GPa)	Poisson's ratio	Yield stress (MPa)	Coefficient of thermal expansion 10^{-6} K^{-1}
Coating	ASTM 301	207	0.29	450	16.9
Bond coat	Ni–Al	182[34]	0.32	–	11.9[35]
Substrate	ASTM 2017A	72.5	0.33	212	22.9

Table 2. Coating composition: ASTM 301.

Component	C	Si	Mn	P	Cr	Ni	Mo	Fe
%	<0.1	<0.5	0.7	0.01	18	8	<0.5	Rest

Table 3. Substrate composition: ASTM 2017A.

Component	Si	Fe	Ti	Cu	Mn	Mg	Zn	Cr	Al
%	0.5	0.58	–	4.58	0.41	0.93	0.21	0.093	92.68

the ASTM E837–13 standards regarding the tolerance on the hole diameter and maximum investigated depth are respected.

The choice of the depth increment depends on whether the specimen is thin or thick. Specimens are considered thin when the thickness is less than $0.4 \times D$. If the thickness is greater than $1.2 \times D$, the specimen is considered thick. For the latter case, a minimum of eight sets of strain readings are measured as the hole depth is increased in equal increments of $0.05 \times D$ or less up to the maximum investigated depth of 800 µm. In this study, all specimens are thick. The maximum increment size is computed from $0.05 \times 2 = 100$ µm. For better in-depth stress details, an increment hole depth of 50 µm is used.

Since the measured strains using the incremental HDM are typically of a few µm/m, correct bonding roughness of 3.5 µm is obtained by means of sand paper. Surfaces are cleaned from all contaminants and dust with an HBM liquid without altering surface stresses. Strain gage rosettes installation, bonding and wire soldering are carried out with respect to the prescription of the ASTM E837–13 standard. Drilling sequences are performed with a high-velocity electric drilling machine (Roland MDX500) of 48,000 r/min, a resolution of 10 µm in x, y, z directions and a position precision of ±0.1 mm/300 mm.

According to the stain gage rosette geometry, a high hardness stainless steel drill shank of 2 mm in diameter is used. The drilling sequence is

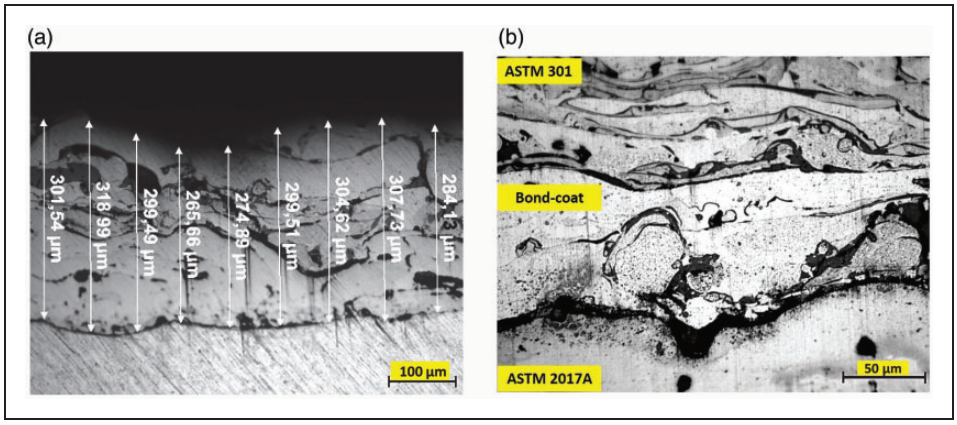

Figure 2. Metallographic images of a wire arc sprayed stainless steel (ASTM 301) on aluminium substrate (ASTM 2017A). (a) Example of a 300 µm coating thickness. (b) Illustration of the layered structure of the coating.

Table 4. Wire arc spraying parameters.

Air pressure in the engine	Air pressure in spray nozzle	Speed rate of the metallic wire	Generator voltage	Current intensity
3.8 bars	3 bars	0.06 m/s	30–32 V	100–120 A

Table 5. Experimental wire arc spraying conditions.

Distance	Angle shot	Wire diameter	Arc Temp
140 mm	90°	1.6–2 mm	4000 °C

automatically controlled and carried out in steps of 10 µm until reaching the increment hole depth of 50 µm. Resulting raw strain data are recorded by the strain gage amplifier QuantmX MX 1615B of ±1 µm strains resolution and an acquisition frequency of 300 s^{-1} per channel. To reduce noise, relieved micro strains are smoothed and filtered. Limitation regarding intermediate specimen thickness, $(0.4–1.2) \times D$, reported in the ASTM standard, where results are considered as approximate, is respected by choosing a substrate thickness of 8 mm. Relaxed strains are obtained by a system of three wire quarter bridge strain gage rosettes with a self-compensating temperature shown in Figure 4(a) and 4(b).

An example of a recorded raw strain data is illustrated in Figure 5(a). To reduce micro strains of thermal origins, a latency time of 60 s between each increment of 50 µm is adopted and final strains values are averaged along 60 s as illustrated in Figure 5(b). Zero depth is achieved by an electrical contact system and coaxiality is ensured by an optical microscope housed in a special drilling head. At the end of the drilling sequences, a hole diameter of 2.1 mm is measured.

Residual stress calculation

Integral method

As mentioned earlier, the integral method is the most used technique for computing stress fields when they are supposed to vary considerably through the thickness. Stress values are computed from the relaxed strain data at various depths based on the following set of integral equation (1)

$$\begin{cases} \boldsymbol{p}(h_i) = \dfrac{1+\nu}{E}\displaystyle\int_0^{h_i} \hat{A}(H,h_i)\ \boldsymbol{P}(H)\mathrm{d}H \\ \boldsymbol{q}(h_i) = \dfrac{1}{E}\displaystyle\int_0^{h_i} \hat{B}(H,h_i)\ \boldsymbol{Q}(H)\mathrm{d}H \quad 0 \leqslant H \leqslant h \\ \boldsymbol{t}(h_i) = \dfrac{1}{E}\displaystyle\int_0^{h_i} \hat{B}(H,h_i)\ \boldsymbol{T}(H)\mathrm{d}H \end{cases} \tag{1}$$

For the sake of simplicity, the strains and stresses in equation (1) may be decoupled using the transformations of stress and strain variables given by equations (2) and (3). These latter give the mathematical formulas of the combined stresses and strains respectively.

$$\boldsymbol{P}_j = \frac{\sigma_{1,j}+\sigma_{3,j}}{2}, \quad \boldsymbol{Q}_j = \frac{\sigma_{3,j}-\sigma_{1,j}}{2}, \quad \boldsymbol{T}_j = \tau_{13,j} \tag{2}$$

$$\boldsymbol{p}_i = \frac{\varepsilon_{1,i}+\varepsilon_{3,i}}{2}, \quad \boldsymbol{q}_i = \frac{\varepsilon_{3,i}-\varepsilon_{1,i}}{2}, \quad \boldsymbol{t}_i = \frac{\varepsilon_{3,i}+\varepsilon_{1,i}-2\varepsilon_{2,i}}{2} \tag{3}$$

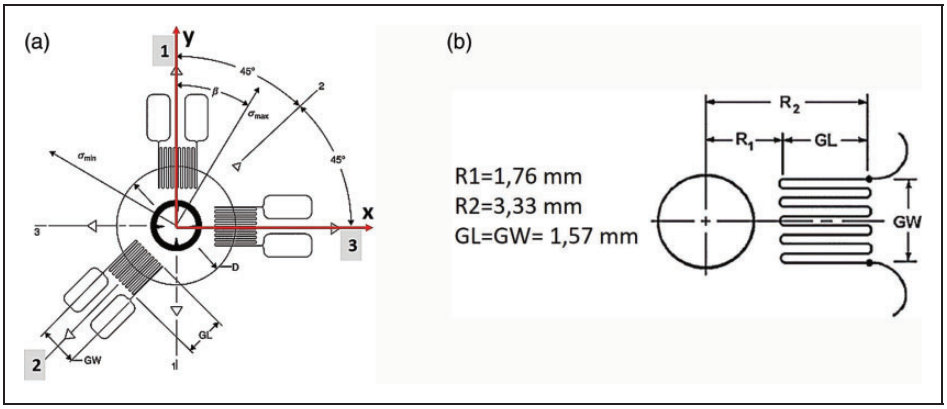

Figure 3. Geometric representation of the used strain gage rosette. (a) Schematic representation of strain gage rosette employed for the measurement of strain relaxation. (b) Used symbols for the rosette geometry definition.

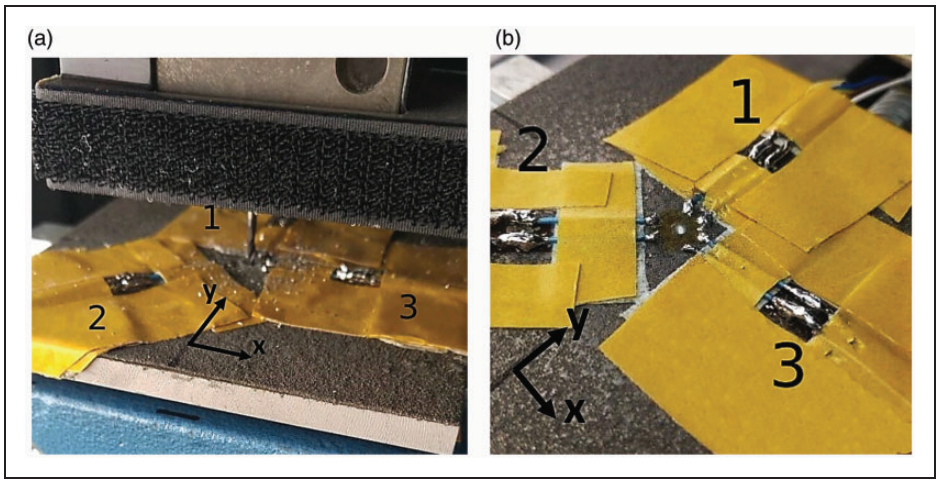

Figure 4. Experimental setup. (a) Hole-drilling device. (b) Reference system for stress state calculation.

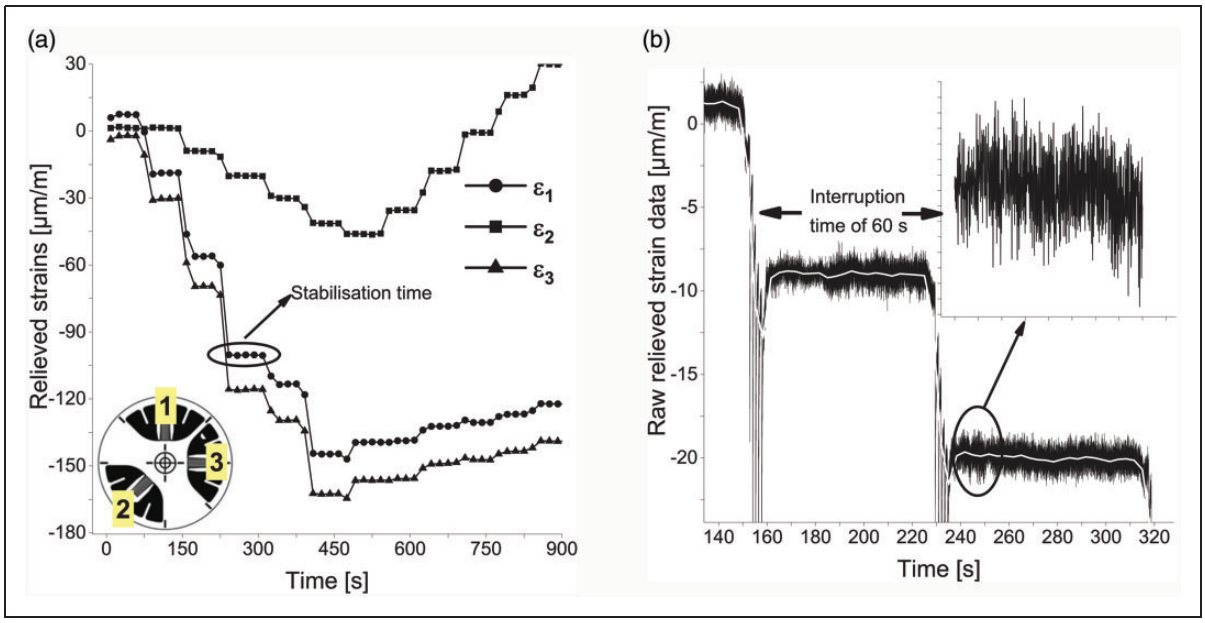

Figure 5. Strain measurements. (a) Example of raw strain data. (b) Range of average strains measurement.

where $\boldsymbol{p}$ represents the components of the mean volumetric strain relaxations and $\boldsymbol{P}$ is the corresponding residual stresses. Similarly, $\boldsymbol{q}$, $\boldsymbol{Q}$, $\boldsymbol{t}$ and $\boldsymbol{T}$ represent the shear strain and stress components at 45°, and the shear strain and shear stress components in x and y direction, respectively. Considering the reference system of the rosette geometry shown in Figure 4(a), ε_1, ε_2 and ε_3 represent the relieved strains measured by the strain gage grids. σ_1, σ_3 and τ_{13} are the generic plane stress corresponding to the individual strain gage readings at each hole depth. $\hat{\boldsymbol{A}}$ and $\hat{\boldsymbol{B}}$ are, respectively, the cumulated strain relaxation functions for hydrostatic and shear stress state per unit depth caused by a unit stress at depth H when the hole depth is h as shown in Figure 6(a). Equation (4) gives an integral formulation of the calibration coefficients $\hat{\boldsymbol{A}}$ and $\hat{\boldsymbol{B}}$.

$$\begin{cases} \hat{A}(H,h) = \int_0^H \hat{A}(H,h)\,\mathrm{d}H \\ \hat{B}(H,h) = \int_0^H \hat{B}(H,h)\,\mathrm{d}H \end{cases} \tag{4}$$

In practice, the strain relaxations are measured after increasing the hole depth in n discrete increments to depth $h_i = 1, 2, \ldots, n$. The integral method consists of transforming the continuous problem described in equation (1) into a set of discrete equations given in equation (5)

$$\begin{cases} \sum_{j=1}^{j=i} \overline{\mathbf{a}}_{\mathbf{ij}}\ \boldsymbol{P}_j = \frac{E}{1+\nu}\ \boldsymbol{p}_i \\ \sum_{j=1}^{j=i} \overline{\mathbf{b}}_{\mathbf{ij}}\ \boldsymbol{Q}_j = E\ \boldsymbol{q}_i \quad 1 \leqslant j \leqslant i \leqslant n \\ \sum_{j=1}^{j=i} \overline{\mathbf{b}}_{\mathbf{ij}}\ \boldsymbol{T}_j = E\ \boldsymbol{t}_i \end{cases} \tag{5}$$

Non-dimensional coefficients $\overline{\mathbf{a}}_{\mathbf{ij}}$ and $\overline{\mathbf{b}}_{\mathbf{ij}}$ represent the strain relaxation after material removal. Physical interpretation of the calibration coefficients is shown in Figure 6(b). These coefficients are lower triangular matrices and are related to the cumulated strain relaxation functions by equation (6)

$$\begin{cases} \overline{\mathbf{a}}_{\mathbf{ij}} = \int_{H_{j-1}}^{H_j} \hat{A}(H,h_i)\,\mathrm{d}H = \hat{A}(H_j,h_i) - \hat{A}(H_{j-1},h_i) \\ \overline{\mathbf{b}}_{\mathbf{ij}} = \int_{H_{j-1}}^{H_j} \hat{B}(H,h_i)\,\mathrm{d}H = \hat{B}(H_j,h_i) - \hat{B}(H_{j-1},h_i) \end{cases} \tag{6}$$

By solving the three matrix systems defined in equation (5), the unknown vectors ($\boldsymbol{P}_j$, $\boldsymbol{Q}_j$ and $\boldsymbol{T}_j$) are found and stress distributions are obtained for each depth j in the coordinate system of the gages. It is important to mention that elastic properties defined in Table 1 and used in equation (5) depend on whether the drilling sequence has reached the substrate, bond coat or coating. Also, the resulting stress values are the equivalent uniform stress within each hole depth increment.

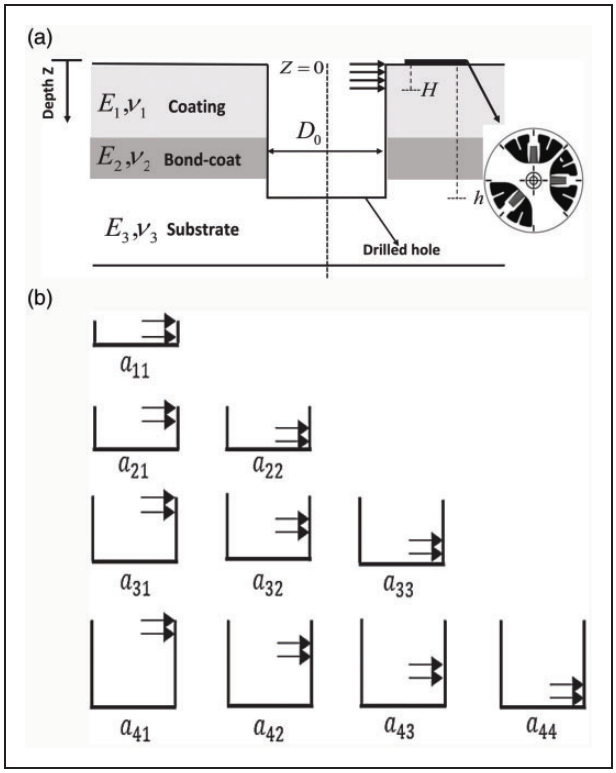

Figure 6. Integral method. (a) Schematic representation of the integral hole drilling method. (b) Physical interpretation of calibrations coefficients.

Calculation of calibration coefficients

As discussed in the introduction, in the case of layered systems and blind hole drilling procedure, coefficients $\hat{\boldsymbol{A}}$ and $\hat{\boldsymbol{B}}$ cannot be directly computed from theoretical considerations. A Computer program is developed using Abaqus software to simulate the integral hole drilling process. A 3D finite element model is used for calibration matrices $\overline{\mathbf{a}}_{\mathbf{ij}}$ and $\overline{\mathbf{b}}_{\mathbf{ij}}$ calculation. With the 3D model, matrices $\overline{\mathbf{a}}_{\mathbf{ij}}$ and $\overline{\mathbf{b}}_{\mathbf{ij}}$ are determined within one computation procedure. Another advantage of the 3D model lies in the fact that it is more realistic since the real constrain conditions cannot be simulated by the 2D model. A Python routine is developed so that the calibration coefficients and residual stresses corresponding to sample geometry dimensions, materials properties, drilled hole radius, load magnitude and mesh scheme are obtained. The simulated drilling sequence is chosen to correspond exactly to the experimental one. Coefficients $\hat{\boldsymbol{A}}$ and $\hat{\boldsymbol{B}}$ are then evaluated without resorting to interpolations. Several simplifying assumptions are assumed:

(a) Sample geometry corresponds to plane plates of 100 mm^2. In this case, plane stress state is considered for the stress calculation.

(b) The adhesion between substrate, bond coat and coating is supposed perfect, material behaviour during the drilling sequence is assumed linear isotropic and no plastic behaviour is taken into account.
(c) All displacements are continuous at the interface between the coating and the substrate.
(d) The determined residual stresses are less than the yield stress of the coating material.

For symmetry considerations, only a quarter of the 3D model represented in Figure 7(a) is considered. All samples are modelled with structural eight nodes linear hexahedral C3D8R element type. The in-depth mesh size is chosen to be at least equal to the minimum between the hole increment 50 µm and the thickness of the bond coat 90 µm. Therefore, an in-depth mesh size of 25 µm is used. For the bond-coat layer, a through thickness mesh density of five equi-sized elements is adopted. The total number of elements in the bond-coat layer is 10,645. Based on a preliminary parametric study on mesh convergence, hole surrounded and strain gage areas are assigned a very fine and regular mesh whereas larger volume elements are selected as the distance from the hole centre increases as shown in Figure 7(a). Finer meshes are investigated and results are found practically unaffected. Figure 7(c) illustrates the in-depth considered element size. The displacement along the z direction of the bottom surface (1) is set to zero. Due to symmetry, the displacements of surfaces (2) and (3) along the y and x axes are null (Figure 7(b)). In order to simulate the conditions of an infinite plate, surfaces (4) and (5) are fixed in all directions. Figure 7(b) summarizes the boundary conditions applied to the quarter of the finite element model. To obtain $\overline{\mathbf{a}}_{ij}$ and $\overline{\mathbf{b}}_{ij}$ in one calculation, a uniform stress field is applied to the 3D FE model as shown in Figure 7(c). Loading conditions and strains relaxation in the simulated model (caused by drilling a hole in a coating system) are applied on the inside surface of the drilled hole. The strains, measured by the strain gage rosettes, are obtained by averaging the radial displacement over the nodes representing the strain gage rosette area (see Figure 7(a)). Figure 8(a) and 8(b) shows an example of the obtained displacement response under the

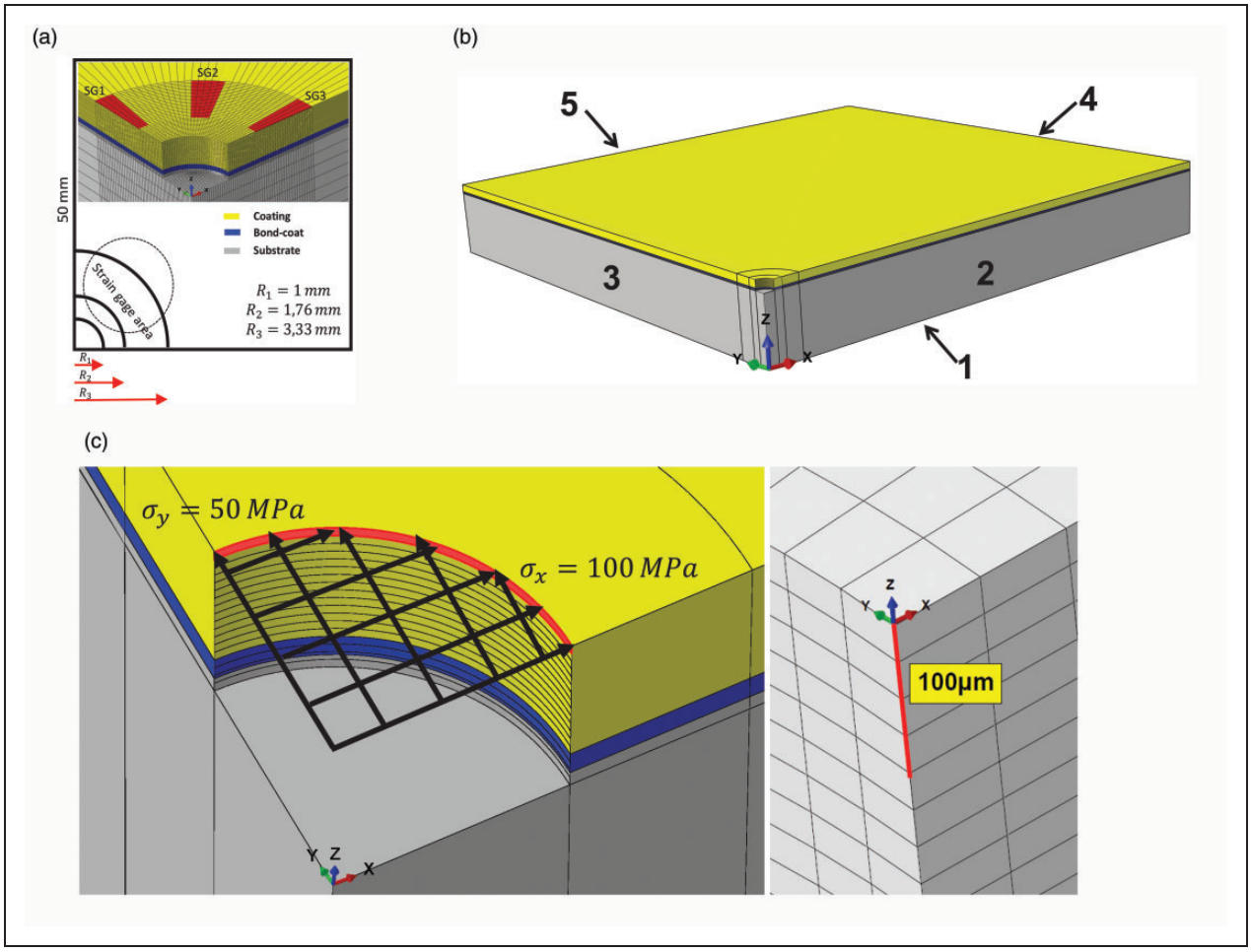

Figure 7. Three-dimensional finite element model used for the calculation of the calibration coefficients (Abaqus software). (a) 3D quarter finite element model and strain gages positions. (b) Finite element model constraints. (c) Calibration loading and in-depth mesh metrics.

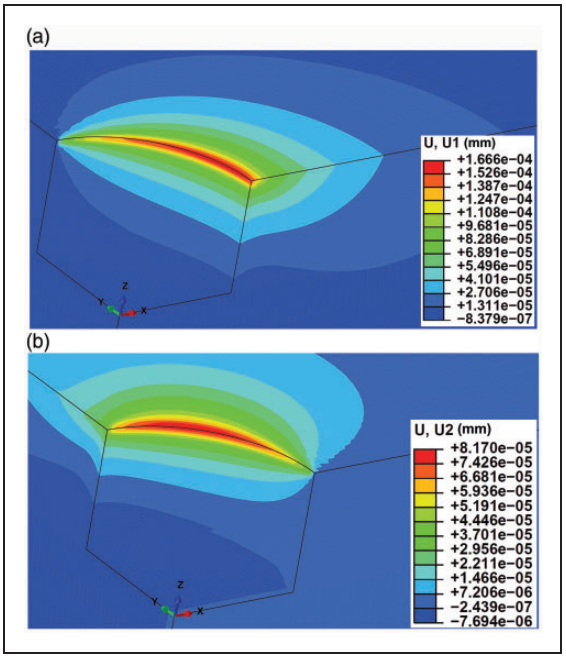

Figure 8. Distributions of the displacement fields under the loading conditions. (a) Radial pressure. (b) Transversal pressure.

loading conditions. The residual stresses are back computed using equation (7) which is derived from the system of the discrete equation (5).

$$\begin{cases} \overline{\mathbf{a}}_{\mathbf{ij}} = \dfrac{E}{1+\nu} \quad \dfrac{\varepsilon_{1ij}+\varepsilon_{3ij}}{\sigma_{1ij}+\sigma_{3ij}} \\ \overline{\mathbf{b}}_{\mathbf{ij}} = E \quad \dfrac{\varepsilon_{3ij}-\varepsilon_{1ij}}{\sigma_{3ij}-\sigma_{1ij}} \end{cases} \tag{7}$$

where $\sigma_{1ij} = 100$ MPa and $\sigma_{3ij} = 50$ MPa represent the applied calibration loads in direction of gages 1 and 3, respectively. ε_{1ij} and ε_{3ij} are the averaged strains over the gage rosette area in red bold.

Results and discussions

Figure 9 shows relaxed strains distribution data for the four coating thicknesses evaluated. Results are interpolated with polynomial functions of different orders. As shown in Figure 5(b) and during the drilling period, the released strains are fluctuating. Whereas, during the time of strain release (interruption time), strains have reached relatively damped

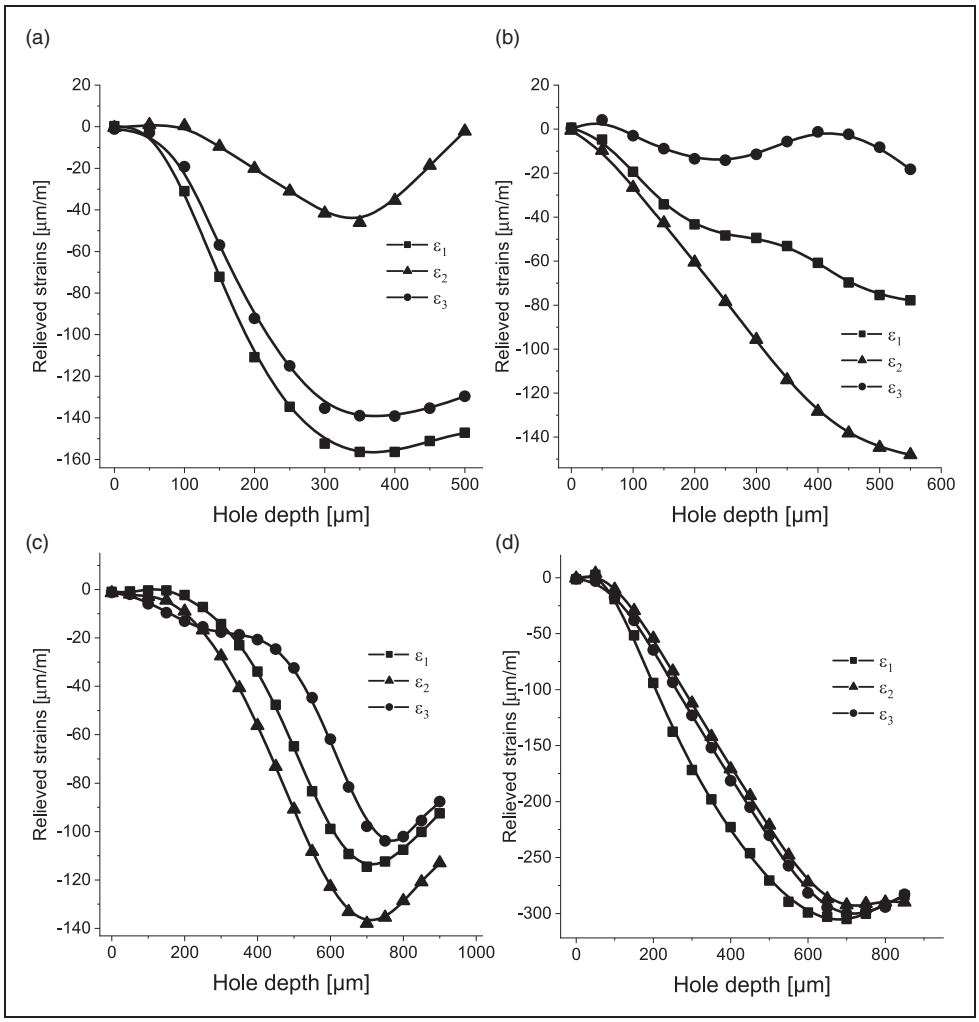

Figure 9. Measured relaxed strains for different thicknesses. (a) 300 μm. (b) 350 μm. (c) 700 μm. (d) 750 μm.

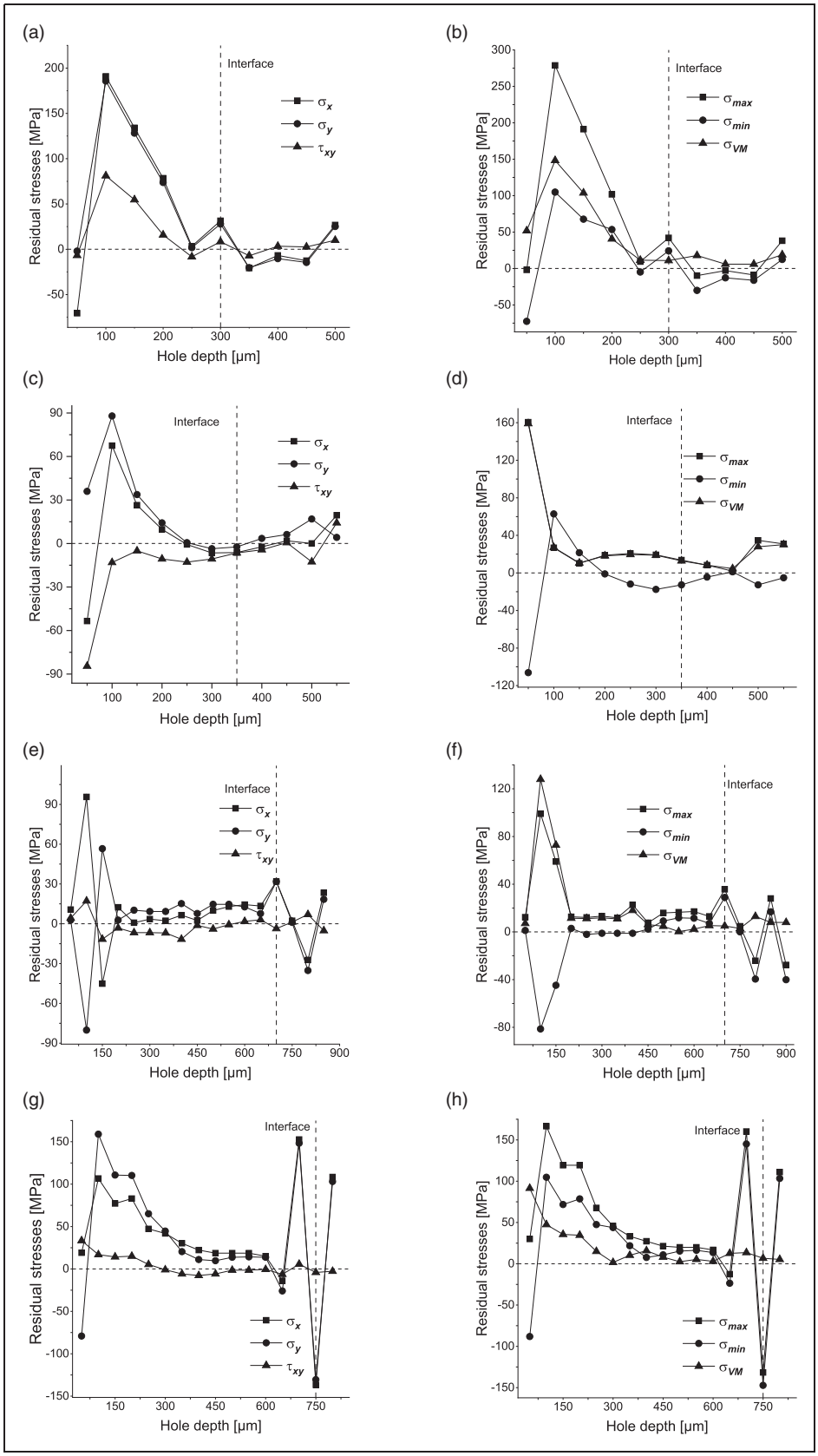

Figure 10. Residual stress distributions for different thicknesses. (a), (c), (e) and (g): normal and shear stresses components. (b), (d), (f) and (h): Principal and Von Mises equivalent residual stresses.

variations. It can be observed that, for all coating thicknesses, the relieved relaxed strains are negative, denoting the development of tensile residual stresses. The relaxed strains evolve in two stages:

1. A decrease from the top surface to the coating/substrate interface.
2. An increase from the interface to the substrate.

The approximate 90 μm Ni–Al bond-coat thickness seems to not have an influence on the relaxed strains. According to the strain gage system reference shown in Figure 4(b), ε_1 and ε_3 exhibit the same features for almost all thicknesses. A maximum compressive strain from −300 μm/m to −150 μm/m is observed for all the cases.

For each sample thickness, longitudinal and transversal stresses across the deposits thicknesses have a consistent trend. The scatter of the σ_x and σ_y distributions, over a superficial zone of approximately 200 μm from the top surface of the coating, increase with increasing coating thickness. Except for the first incremental layers, where the shearing stress τ_{xy} is a little significant compared to the longitudinal and transversal stresses in the same layer. Its magnitude is always smaller as shown in Figure 10(a), (c), (e) and (g) and it has an average value that converge to zero. For 700 μm/m and 750 μm/m samples, stress profiles are oscillating. This could be explained by the increased number of drilled hole (15 and 16) increments which leads to a loss of sensitivity in term of the quality of the relaxed strains.[36] The small number of calculation increments (6 and 7), in the case of 300 μm/m and 350 μm/m coating thickness sample, yield a satisfactory level of details, and stress distributions are more smooth and homogeneous. In order to overcome the reduced sensitivity with hole depth, Grant et al.[36] suggest increasing the size of calculation increments at greater depths. The obtained stress distributions are typical for wire arc sprayed deposits. In fact, these deposits are characterized by a high tensile top surface stress and much lower values in the substrate. Through-thickness residual stress profiles represented in Figure 10(b), (d), (f) and (h) for all samples thicknesses show the same trend and agree with those reported by Sampath et al.[37] and Greving et al.[38] The maximum residual stress values vary between 140 and 275 MPa. It should be pointed out that for all thicknesses, the obtained stress values did not exceed the yield stress of the coating. Particular emphasis is placed on the abrupt change in stress sign from tensile to compressive in the case of the 750 μm/m sample thickness. For thicker coatings, a gradual deposition may result in a significant stress gradient across the thickness. Also, this observation could be explained by the contribution of several phenomena that take place at the same time. Firstly, the creation of a compressive stress zone by the sandblasting operation before the deposition process. Secondly, plastic deformation stemming from the blasting conditions and the combination of residual stresses from quenching and thermal origins due to the mismatch of the coefficients of thermal expansion of the coating, bond coat and substrate. Such a change in the computed stress leads to a severe solicitation at the interface and affects its adhesion. Figure 11 shows the evolution of the mean equivalent Von Mises stress acting on the coatings with respect to thickness. It is concluded that the mean equivalent Von Mises stress on the coating decreases with increasing thickness. This leads to a reduction of the interfacial adhesion energy which could nurture debonding. These findings are coherent with those reported by Greving et al. for wire arc thermal-sprayed systems.[38]

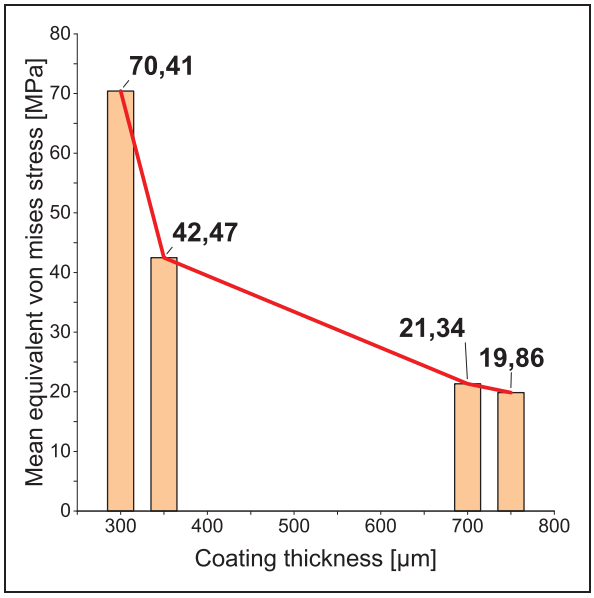

Figure 11. Mean equivalent Von Mises stress with respect to coating thickness.

Conclusion

The present study deals with the effect of wire arc sprayed coating thickness on the in-depth resulting residual stresses. Aeronautical aluminium alloy (ASTM 2017A) substrates were first coated with an Ni–Al bond coat to improve bonding strength. A layered structure of an austenitic stainless steel (ASTM 301) is obtained by gradual deposition with a system of different passes. The sign and residual stress levels have a major effect on the performance of thermally sprayed coatings. Gradual deposition appears to lead to the development of non-uniform stress profiles across the thickness.

The incremental hole-drilling method is a powerful technique for measuring such a residual stress distribution and especially for determining the in-depth profile. Stress-strain transformation formalism based on the integral method is chosen since it is able to decode relaxed strains relating to highly non-uniform residual stress fields. The main advantage of this

method is the simultaneous consideration of the stresses contribution, at all depths, to the total measured strain relaxations. However, a finite element analysis is necessary to accurately calibrate the stress contribution. Therefore, the calibration coefficients related to the relaxed strains and caused by the removal of material layers, are obtained for the specific experimental conditions (materials properties and samples dimensions). Relieved relaxed strains are all negative, indicating the arising of tensile stresses across the coatings thickness. In fact, the average Von Mises residual stress acting on the deposits is tensile as a result of consecutive deposition of layers with tensile quenching stress. This value tends to decrease with the increase in the coating thickness. These findings could explain the loss in the interfacial adhesion energy.

At higher depths, it is shown that the residual stress distributions are fluctuating and abrupt changes from tensile to compressive are observed in the vicinity of the interface. Such behaviour is explained by the sensitivity to strain measurement errors due to the numerical ill conditioning of equation (5). To address this drawback, and improve results, it is recommended to propose an optimization approach regarding the drilling sequence to minimize strain measurement errors.

Acknowledgements

The authors acknowledge ALGERIA METALLISATION company located at Hamadi (Rouiba Algiers) for the grateful help in elaborating all the used samples in the study. Also, we thank the FAST laboratory (Paris, Saclay university, FRANCE) where all measurements concerning the incremental hole drilling procedure were done. The authors would also like to thank Lionel Auffray and Alban Aubertin for technical support.

Declaration of Conflicting Interests

The author(s) declared no potential conflicts of interest with respect to the research, authorship, and/or publication of this article.

Funding

The author(s) received no financial support for the research, authorship, and/or publication of this article.

ORCID iD

Hattali Lamine https://orcid.org/0000-0002-8298-9160

References

1. Tejero-Martin D, Rad MR, McDonald A, et al. Beyond traditional coatings: a review on thermal-sprayed functional and smart coatings. *J Therm Spray Technol* 2019; 28: 598–644.
2. Kahraman N and Gülenç B. Abrasive wear behaviour of powder flame sprayed coatings on steel substrates. *Mater Design* 2002; 23: 721–725.
3. Rodriguez J, Martin A, Fernández R, et al. An experimental study of the wear performance of nicrbsi thermal spray coatings. *Wear* 2003; 255: 950–955.
4. Matthews S, James B and Hyland M. Microstructural influence on erosion behaviour of thermal spray coatings. *Mater Charact* 2007; 58: 59–64.
5. Du H, Sun C, Hua W, et al. Structure, mechanical and sliding wear properties of wc–co/mos2–ni coatings by detonation gun spray. *Mater Sci Eng A* 2007; 445: 122–134.
6. Zeng Zs, Sakoda N and Tajiri T. Corrosion behavior of wire-arc-sprayed stainless steel coating on mild steel. *J Therm Spray Technol* 2006; 15: 431–437.
7. Sova A, Grigoriev S, Okunkova A, et al. Cold spray deposition of 316l stainless steel coatings on aluminium surface with following laser post-treatment. *Surf Coat Technol* 2013; 235: 283–289.
8. Spencer K and Zhang MX. Optimisation of stainless steel cold spray coatings using mixed particle size distributions. *Surf Coat Technol* 2011; 205: 5135–5140.
9. Hattali M, Valette S, Ropital F, et al. Calculation and experimental determinations of the residual stress distribution in alumina/ni/alumina and alumina/ni/nickel alloy systems. *J Mater Sci* 2010; 45: 4133–4140.
10. Laribi M, Mesrati N, Vannes A, et al. Metallurgical characterization and determination of residual stresses of coatings formed by thermal spraying. *J Therm Spray Technol* 2003; 12: 234–239.
11. Schajer GS. *Practical residual stress measurement methods*. New York: John Wiley & Sons, 2013.
12. Alegre J, Díaz A, Cuesta I, et al. Analysis of the influence of the thickness and the hole radius on the calibration coefficients in the hole-drilling method for the determination of non-uniform residual stresses. *Exp Mech* 2019; 59: 79–94.
13. Klein CA. How accurate are Stoney's equation and recent modifications. *J Appl Phys* 2000; 88: 5487–5489.
14. Clyne T and Gill S. Residual stresses in thermal spray coatings and their effect on interfacial adhesion: a review of recent work. *J Therm Spray Technol* 1996; 5: 401.
15. Bolelli G, Candeli A, Koivuluoto H, et al. Microstructure-based thermo-mechanical modelling of thermal spray coatings. *Mater Design* 2015; 73: 20–34.
16. Lima C, Nin J and Guilemany J. Evaluation of residual stresses of thermal barrier coatings with hvof thermally sprayed bond coats using the modified layer removal method (mlrm). *Surf Coat Technol* 2006; 200: 5963–5972.
17. Greving D, Rybicki E and Shadley J. Through-thickness residual stress evaluations for several industrial thermal spray coatings using a modified layer-removal method. *J Therm Spray Technol* 1994; 3: 379.
18. Buchmann M, Gadow R and Tabellion J. Experimental and numerical residual stress analysis of layer coated composites. *Mater Sci Eng A* 2000; 288: 154–159.
19. Held E and Gibmeier J. Application of the incremental hole-drilling method on thick film systems-an approximate evaluation approach. *Exp Mech* 2015; 55: 499–507.
20. ASTM E. *837-13a standard test method for determining residual stresses by the hole drilling strain-gage method*. West Conshohocken: ASTM International, 2013.
21. Montay G, Cherouat A, Lu J, et al. Development of the high-precision incremental-step hole-drilling method for the study of residual stress in multi-layer materials: influence of temperature and substrate on zro2–y2o3 8 wt.% coatings. *Surf Coat Technol* 2002; 155: 152–160.

22. Sicot O, Gong XL, Cherouat A, et al. Influence of experimental parameters on determination of residual stress using the incremental hole-drilling method. *Compos Sci Technol* 2004; 64: 171–180.
23. Valente T, Bartuli C, Sebastiani M, et al. Implementation and development of the incremental hole drilling method for the measurement of residual stress in thermal spray coatings. *J Therm Spray Technol* 2005; 14: 462–470.
24. Nickola W. Practical subsurface residual stress evaluation by the hole drilling method. In: *Proceedings of the spring conference on experimental mechanics*, New Orleans, June 1986, pp.8–13.
25. Schajer G. Measurement of non-uniform residual stresses using the hole-drilling method. Part i-stress calculation procedures. *J Eng Mater Technol* 1988; 110: 338–343.
26. Schajer G. Measurement of non-uniform residual stresses using the hole-drilling method. Part ii-practical application of the integral method. *J Eng Mater Technol* 1988; 110: 344–349.
27. Flaman MT. Brief investigation of induced drilling stresses in the center-hole method of residual-stress measurement. *Exp Mech* 1982; 22: 26–30.
28. Lord J, Fry A and Grant P. *A UK residual stress intercomparison exercise-an examination of the XRD and hole drilling techniques*. Teddington: National Physical Laboratory, 2002.
29. Nau A, von Mirbach D and Scholtes B. Improved calibration coefficients for the hole-drilling method considering the influence of the poisson ratio. *Exp Mech* 2013; 53: 1371–1381.
30. Xiao B, Li K and Rong Y. Automatic determination and evaluation of residual stress calibration coefficients for hole-drilling strain gage integral method. *Strain* 2011; 47: e525–e534.
31. Micro-Measurements V. Measurement of residual stresses by the hole drilling strain gage method. *Tech Note TN* 2010; 503: 19–33.
32. Aoh JN and Wei CS. On the improvement of calibration coefficients for hole-drilling integral method: part i-analysis of calibration coefficients obtained by a 3-d fem model. *J Eng Mater Technol* 2002; 124: 250–258.
33. Standard N. Surface preparation and protective coating. *NORSOK M-501*, Norway, 2012.
34. Mukherjee B, Kumar R, Islam A, et al. Evaluation of strength-ductility combination by in-situ tensile testing of graphene nano platelets reinforced shroud plasma sprayed nickel-aluminium coating. *J Alloys Comp* 2018; 765: 1082–1089.
35. Wang Y, Liu ZK and Chen LQ. Thermodynamic properties of al, ni, nial, and ni3al from first-principles calculations. *Acta Materialia* 2004; 52: 2665–2671.
36. Grant P, Lord J and Whitehead P. *Measurement good practice guide no. 53-issue 2: the measurement of residual stresses by the incremental hole drilling technique*. Teddington: National Physical Laboratory, 2006.
37. Sampath S, Jiang X, Matejicek J, et al. Role of thermal spray processing method on the microstructure, residual stress and properties of coatings: an integrated study for ni–5 wt.% al bond coats. *Mater Sci Eng A* 2004; 364: 216–231.
38. Greving D, Shadley J and Rybicki E. Effects of coating thickness and residual stresses on the bond strength of astm c633-79 thermal spray coating test specimens. *J Therm Spray Technol* 1994; 3: 371.

Appendix

Notation

$\hat{\boldsymbol{A}}$, $\hat{\boldsymbol{B}}$	cumulated strain relaxation functions for hydrostatic and shear stresses states
$\overline{\mathbf{a}}_{\mathbf{ij}}$, $\overline{\mathbf{b}}_{\mathbf{ij}}$	calibration matrices for isotropic and shear stresses states
D	diameter of the drilled hole
Ra	surface roughness
E	Young's modulus
h	hole depth
H	depth
$\boldsymbol{P}$, $\boldsymbol{p}$	uniform isotropic stress and corresponding strain
$\boldsymbol{Q}$, $\boldsymbol{q}$	uniform shear 45° stress and corresponding strain
$\boldsymbol{T}$, $\boldsymbol{t}$	uniform shear stress in x-y direction and corresponding strain
$\varepsilon_{1,2,3}$	relieved strains measured by the strain gage grids
ν	Poisson ratio
σ_1	ε_1 corresponding stress
σ_3	ε_3 corresponding stress
σ_{max}	maximum principal stress
σ_{min}	minimum principal stress
σ_{VM}	Von Mises stress
τ_{13}	ε_2 corresponding stress
σ_x, σ_y	stresses in x and y direction
τ_{xy}	shear x–y stress